Electronic Supplementary Material (ESI) for Chemical Communications.

Supplementary file

A Bilayer Coating as an Oxygen-Transfer Cascade for the Electrochemical Ambient Conversion of Methane to Oxygenates

Yanir Kadosh,[a] Yeshayahu Ben-Eliyahu,[b] Yair Bochlin,[a] Lior Ezuz,[a] Yacov Iflah,[b] Shuli Halevy,[b] Sebastian Kozuch,[c] Eli Korin[a] and Armand Bettelheim[a].*

[a.]Chemical Engineering Department, Ben-Gurion University of the Negev, Be'er Sheva, 84105, Israel.

[b.]Chemistry Department, Nuclear Research Centre-Negev, Be'er Sheva, 84190, Israel.

[c.]Chemistry Department, Ben-Gurion University of the Negev, Be'er Sheva, 84105, Israel.

*Corresponding author: Prof. Armand Bettelheim, armandb@bgu.ac.il

Table of contents

List of figures

List of tables

1. Materials

Sodium acetate (≥ 99.0%), nickel sulfate (≥ 98.0%) and sodium sulfate (≥ 99.0%) were purchased from Sigma-Aldrich. Indium-tin oxide (ITO) working electrodes were purchased from Sigma-Aldrich. Manganese(III) 5,10,15,20-(tetra-4-hydroxyphenyl)porphyrin chloride (MnTHPP) was obtained from PorphyChem. The structure of the porphyrin is found below in Figure S1.

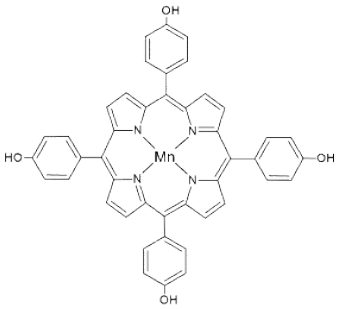

Figure S1. The structure of manganese 5,10,15,20-(tetra-4-hydroxyphenyl) porphyrin.

2. Films deposition

The oxidant layer, which is comprised of the $Ni(OH)_2$/NiOOH redox couple (will be referred as **Ni#**) was obtained by anodic deposition on an ITO transparent working electrode.[1–3] Prior to the anodic deposition, the ITO was washed with acetone, ethanol, and deionized water and was left to dry overnight. All the measured potentials on the Hg/HgO scale were converted to the standard hydrogen electrode (SHE) scale by adding 0.14 V.

The deposition process was conducted by 30 consecutive potential scans from 0.6 to 1.5 V vs. SHE at 25 mV s^{-1} in a solution of 0.13 M sodium acetate, 0.13 M nickel sulfate and

0.1 M sodium sulfate. Then, the coating was aged in 1 M KOH for additional 30 cycles until the current stabilized.

Figure S2A presents the deposition processes of the Ni# film. The process is initiated by the oxidation of Ni^{2+} ions to Ni^{3+} that react afterwards with OH^- ions to form insoluble NiOOH (redox couple of $Ni(OH)_2$/NiOOH is marked as R_1/O_1). These reactions take place on the surface of the ITO working electrode and eventually a film is obtained.

The porphyrin film was obtained by the electropolymerization of MnTHPP (will be referred as **Mn#**).[4] The film was obtained on the ITO working electrode by 20 consecutive potential scans at 25 mV s^{-1} from 0.15 to 1.35 V vs. SHE. The solution was 0.1 M KOH, which contained 0.273 mM of dissolved MnTHPP. After the procedure, the working electrode was soaked in a 0.1 M KOH solution in order to dissolve unreacted MnTHPP from its surface, and then it was washed with deionized water. A green film is obtained after the process.

Figure S2B presents the CV scans of the electropolymerization of MnTHPP on ITO. Applying a sufficient anodic potential initiates the oxidation of the peripheral hydroxyl groups that eventually form covalent bonds between the porphyrin units. This process can be observed notably in the first CV cycle of Figure S2B by the irreversible peak at 0.7 V.[5] As was previously observed for such films, upon continued electropolymerization the current decreases by the formation of a film with a non-conductive nature.[1] After the consecutive CV scans, a green film is observed on the conductive side of the ITO, which was found to be insoluble in the same electrolyte.

The bilayer coating (will be referred as **Ni#/Mn#**) that is comprised of both the oxidant layer and the mediator layer, was first electrodeposited by Ni# and then followed by Mn# deposition on the ITO working electrode. The preparation of the two coatings in a bilayer structure is presented in Figure S2C. The CV curve represents the electropolymerization of the porphyrin when the surface of the ITO was coated first with Ni#. Figure S2D presents an image of the ITO after obtaining the bilayer coating.

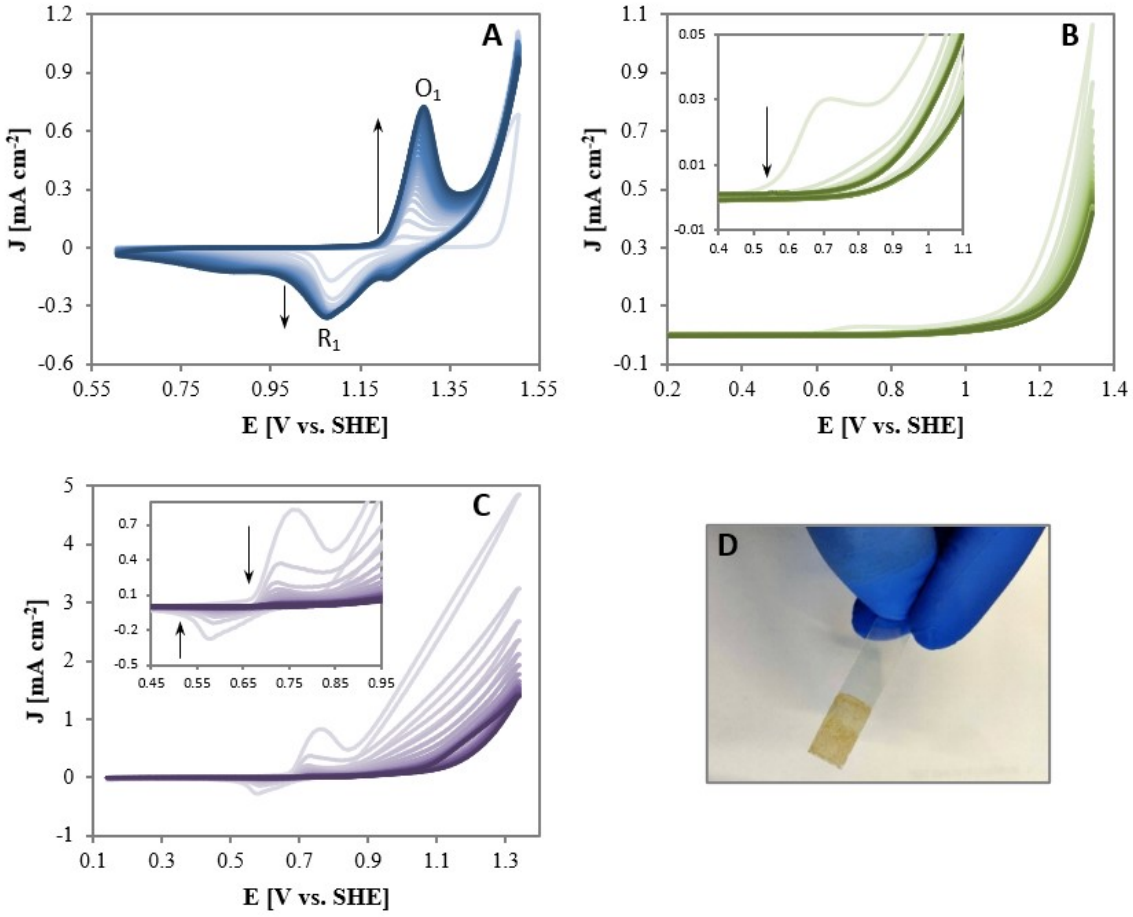

Figure S2. Electrodeposition of the coatings (the brightest and the darkest curves represent the first and the last cycle, respectively). (A) Anodic deposition of Ni# film from a solution of 0.13 M sodium acetate, 0.13 M nickel sulfate and 0.1 M sodium sulfate. (B) MnTHPP electropolymerization from a solution of 0.1 M KOH that contains 0.273 mM of dissolved porphyrin. (C) Bilayer Ni#/Mn# film formation of the two layers, when Ni# is the first layer and Mn# is the second one. Insets presents the zoom-in on the redox potential area. (D) Image of the ITO after obtaining the bilayer coating.

3. Coatings' characterization

The morphology of the coatings was examined by a FEI Verios high resolution scanning electron microscope (HRSEM). Scanning transmission electron microscopy (STEM) imaging and energy dispersive spectroscopy (EDS) for compositional information were conducted by FEI Helios G4 UC extreme high resolution field emission SEM microscope, equipped with focused ion beam (FIB) technology for sample preparation.[6] The sample was first coated with Au layer, followed by Pt layer, which were deposited as protective layers during the FIB fabrication process. X-ray photoelectron spectroscopy (XPS) measurements were performed on a Thermo Fisher Scientific ESCALAB 250 instrument. The UV-Vis absorbance spectra were recorded using Ocean Optics spectrophotometer (DH-2000-BAL) with SpectraSuite data acquisition and analysis software.

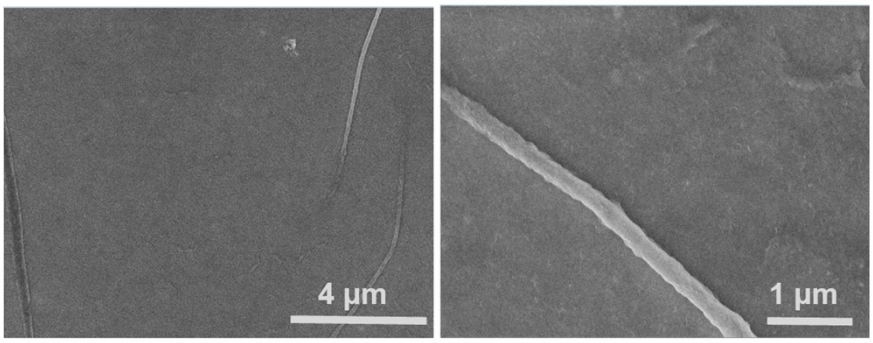

Figure S3. Top view HRSEM images of $Mn^{\#}$ of the bilayer.

Figure S4 presents the bright-field STEM image of the cross section of the bilayer Ni#/Mn# coating and the obtained EDS signals for the various examined elements. The signals/length profiles are according to the direction shown in Figure S4A and start at X_0 and end at the ITO layer on the glass (total length of about 230 nm). The low signal for Mn results from the low concentration of Mn in the coating due to the low Mn atomic weight in comparison to the molecular weight of the porphyrin ligand (Figure S1).

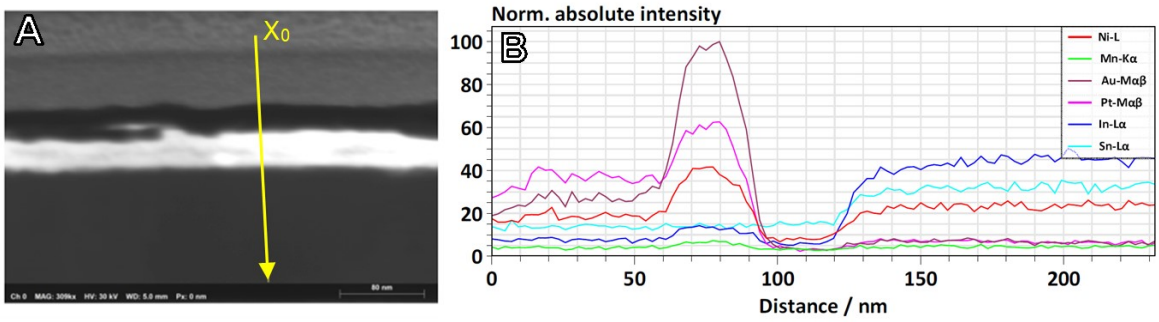

Figure S4. (A) Bright-field STEM image of the cross section of the bilayer film and the corresponding EDS signals (B) of the examined elements along the yellow line in image (A).

Further characterization of the coatings was obtained by UV-Vis spectroscopy. Figure S5 shows a comparison between the UV-Vis absorbance spectra of $Mn^{\#}$ and $Ni^{\#}/Mn^{\#}$ as compared to that of dissolved MnTHPP in methanol. The Soret bands of the electrodeposited MnTHPP in $Mn^{\#}$ and $Ni^{\#}/Mn^{\#}$ are red shifted in comparison to λ_{max} of the dissolved species (481, 478, and 471 nm, respectively), as expected from the effect of the extended conjugated systems in polymeric metalloporphyrins.[7]

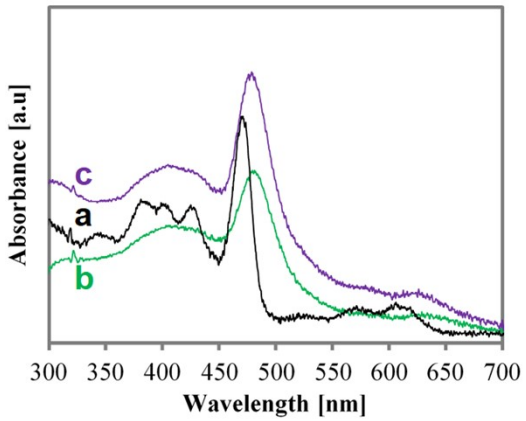

Figure S5. UV-Vis absorbance spectra of (a) MnTHPP dissolved in methanol, (b) $Mn^{\#}$ and (c) $Ni^{\#}/Mn^{\#}$ coatings on ITO.

The chemical composition was investigated by X-ray photoelectron spectroscopy (XPS). Figures S6A and S6B present the Ni 2p and Mn 2p XPS spectra of $Ni^{\#}$ and $Mn^{\#}$, respectively. Sharp peaks of Ni $2p_{3/2}$ and Ni $2p_{1/2}$, with binding energies of 855.7 eV and 873.3 eV, respectively, for Ni^{2+}, and 856.6 eV and 874.5 eV, respectively, for Ni^{3+} can be observed.[8] both for $Ni^{\#}$ and $Ni^{\#}/Mn^{\#}$ (Figures S6A and S6C, respectively). In addition, when inspecting the Mn 2p XPS spectrum for $Ni^{\#}/Mn^{\#}$, two peaks located at 643.5 and 653.6 eV are observed and these are shifted in comparison to those of $Mn^{\#}$ (643.6 and 654.9 eV, Figure S6D). This is attributed to tight proximity of the two layers in $Ni^{\#}/Mn^{\#}$, as also evidenced by the STEM observations (Figure 1D), which probably results in conjugated electronic interactions.[9]

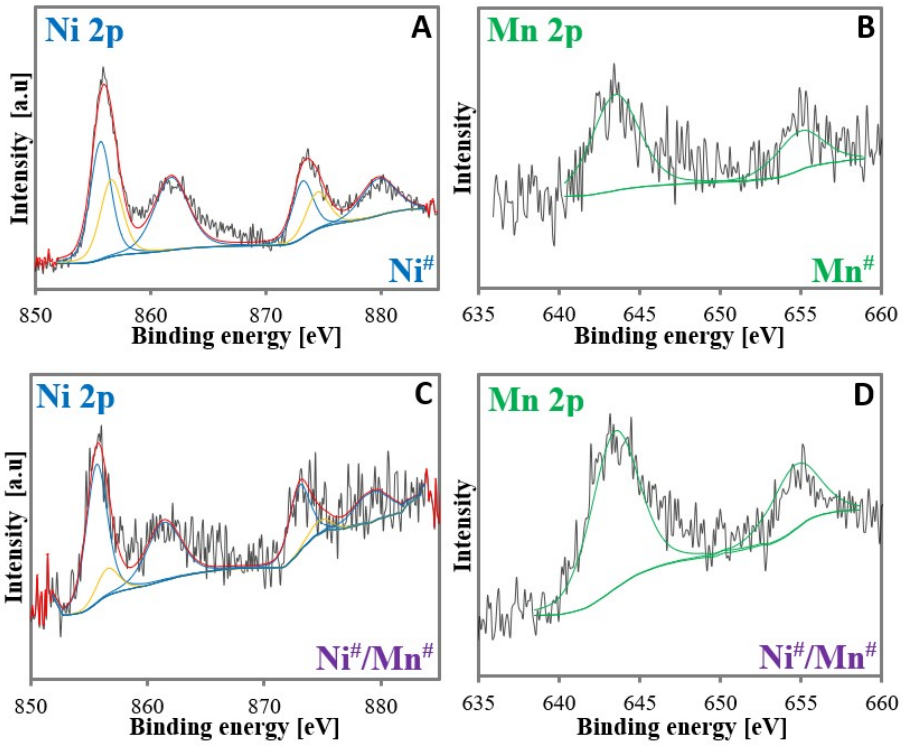

Figure S6. XPS spectra of (A) Ni 2p and (B) Mn 2p of $Ni^{\#}$ and $Mn^{\#}$ coatings, respectively. XPS spectra of (C) Ni 2p and (D) Mn 2p of the $Ni^{\#}/Mn^{\#}$ coating.

4. Electrochemical measurements

The electrochemical experiments were conducted on a Gamry ($G^{TM}300$) potentiostat using a 3-electrode electrochemical cell with an ITO working electrode (1.5 cm^2 geometric surface area), platinum wire (Sigma-Aldrich, 99.9%) auxiliary electrode separated by a fritted glass bridge (PINE) and an Hg/HgO (1 M KOH) reference electrode. All the potentials reported in this work are referred to SHE reference scale. The experiments were conducted in a 0.1 M KOH (pH 13.0) at room-temperature. Cyclic voltammetry (CV) experiments were conducted at various scan rates to characterize the $Ni(OH)_2$/NiOOH couple in Ar saturated electrolyte (Figure S7) and at 25 mV s^{-1} to examine the effect of the presence of CH_4. Ar or CH_4 was purged into the electrolyte for half an hour prior to the measurement. Electrochemical impedance spectroscopy (EIS) measurements were performed at 0.85 V by applying a sinusoidal voltage of 10 mV, and the spectra were recorded in the frequency range from 100 kHz to 0.1 Hz. The EIS 300 software (Gamry) was used for data collection and the obtained impedance plots were fitted by Echem Analyst (Gamry) software.

Products characterization was conducted in a batch mode operation in a sealed 3-electrode cell (Biologic, EL-ELECTRO-2) by applying different potentials (0.9, 0.95, 1.00 and 1.05 V vs. SHE) for 2 hours at 1 atm. Gas samples were taken from the headspace with a 0.5 mL gas-tight syringe (RESTEK) and were injected manually to a gas chromatograph (GC) column equipped with flame ionization (with methanizer) and thermal conductivity detectors. Detection of dissolved oxygen was conducted using a dissolved oxygen probe (Thermo Scientific Orion^{TM}-9708) connected to a pH meter.[10]

Stability of the coatings was examined by CA at 0.95 V for 4 hours with continuous bubbling of methane.

Spectroelectrochemical measurements of the coatings were conducted on ITO in the same conditions used previously in a polystyrene cuvette. The cell was mounted in the cuvette stand while the ITO was positioned in front of the spectrophotometer's beam, and Pt wire and AgCl wire were used as the counter and pseudo-reference electrodes, respectively. The experiments were conducted in an Ar or CH_4 atmosphere by purging the desired gas 15 min prior to the measurement. UV-Vis difference absorbance spectra were plotted at various applied potentials with intervals of 100 mV (from 0.35 V to 1.05 V) by subtracting the measured spectrum at a specific applied potential from the spectrum obtained at 0.25 V vs. SHE.

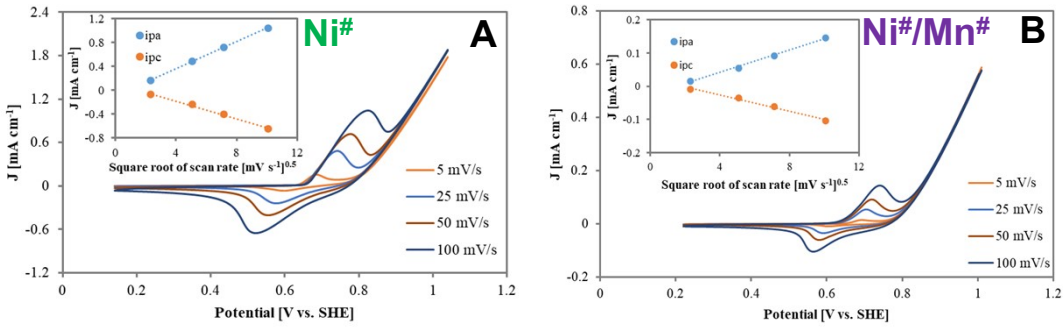

Figure S7. Cyclic voltammograms obtained at different scan rates for the Ni# (A) and Ni#/Mn# (B) coatings in deaerated 0.1 M KOH solution. Insets: plots of anodic and cathodic current densities (ipa and ipc, respectively) vs. square root of scan rate.

As it can be seen in Figure S7, peak shifting toward more positive and negative values of the anodic and cathodic peaks, respectively, is more pronounced as the scan rate increases. This is commonly observed due to the increased internal diffusion resistance that is more prominent at higher scan rates.[11] The linear relation between the

peak current and the square root of the scan rate suggests that the oxidation of $Ni(OH)_2$ to NiOOH:

$$Ni(OH)_2 + OH^- \leftrightarrow NiOOH + H_2O + e^-$$

is a diffusion-controlled process, in which OH^- ions continuously diffuse from the solution bulk to the $Ni(OH)_2$/ NiOOH layer.[9]

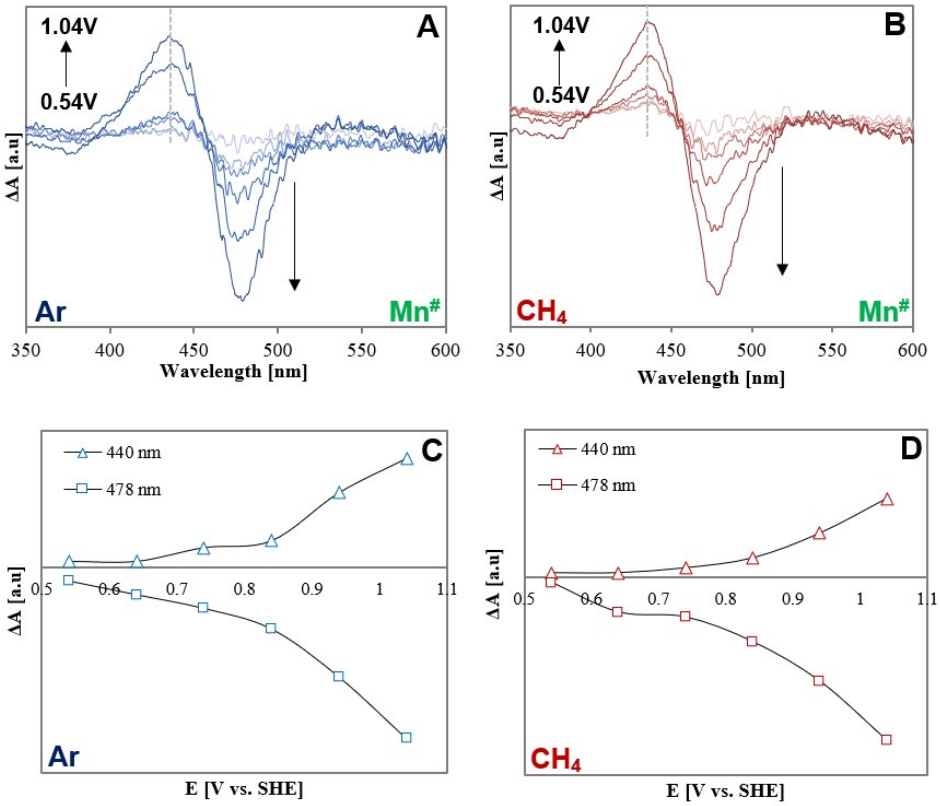

Figure S8. (A & B) Spectroelectrochemistry of Mn# coating in the absence and presence of CH_4, respectively. The UV-Vis difference absorbance spectrum of the coatings on the ITO transparent electrode at various applied potentials with intervals of 100 mV in 0.1 M KOH is displayed (the brightest and the darkest curves represent the initial and the last potential, respectively). In this representation, decaying and growing peaks have negative and positive absorbance, respectively. Images C & D present the difference absorbance profiles as function of the applied potential.

4. Computational details

Density Functional Theory (DFT) computations were performed for the various MnTHPP monomeric complexes expected to be involved in the reactions studied. All computations were made with Gaussian16 software package,[12] with the B3PW91 hybrid functional[13] and the triple ξ 6-311G(d)[14] basis set. In all optimized geometries a full vibrational analysis was carried out to verify the absence of imaginary frequencies. To include the water solvation effect, the conductor like polarized continuum model (CPCM)[15] was used in all the computations. The effects of solute cavitation energy,[16] solute-solvent dispersion and repulsion interactions energies[17] were also included.

Thermochemical computations were carried out at 298.15 K and 1.00 atm. The electrochemical potential in reactions involving electron transitions was calculated from the Gibbs free energy in solution[18] of the products versus reactants, using the thermodynamic relationship to the electrochemical potential: $\Delta G^0 = -nFE^0$ (where n represents the number of electrons passing according to reaction formulation, and F is the Faraday constant). Since the electrochemical potential is always presented as a relative value compared to the reference electrode potential, the standard hydrogen electrode potential (4.44 eV as determined by IUPAC) was subtracted from the calculated potential. The partial atomic charges were computed with natural bonding orbitals (NBO)[19].

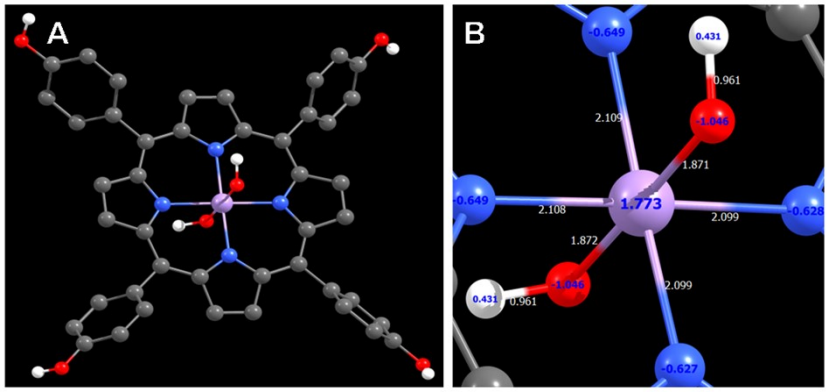

Figure S9. (A) Computed $Mn^{III}THPP(OH)_2$ structure and (B) zoom-in on the metal center with selected bond lengths and atomic charges. Black, blue, red, white and purple represent C, N, O, H and Mn atoms, respectively.

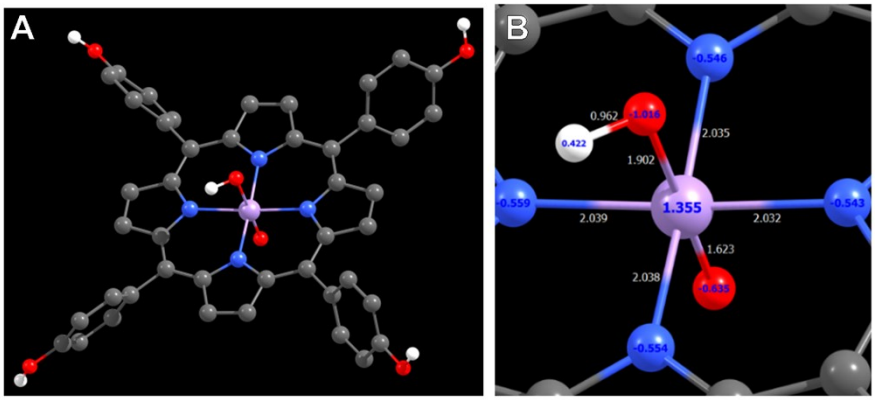

Figure S10. (A) Computed $Mn^{IV}THPP(OH)(O)$ structure and (B) zoom-in on the metal center with selected bond lengths and atomic charges. Black, blue, red, white and purple represent C, N, O, H and Mn atoms, respectively.

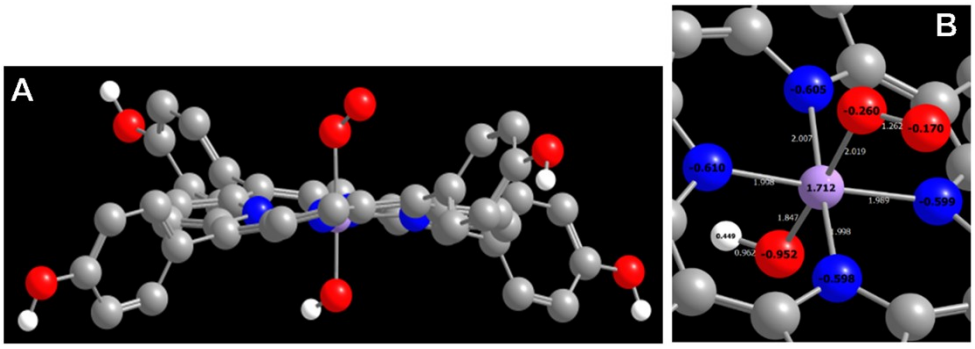

Figure S11. (A) Computed $Mn^{IV}THPP(OH)(OO^{-})$ structure and (B) zoom-in on the metal center with selected bond lengths and atomic charges. Black, blue, red, white and purple represent C, N, O, H and Mn atoms, respectively.

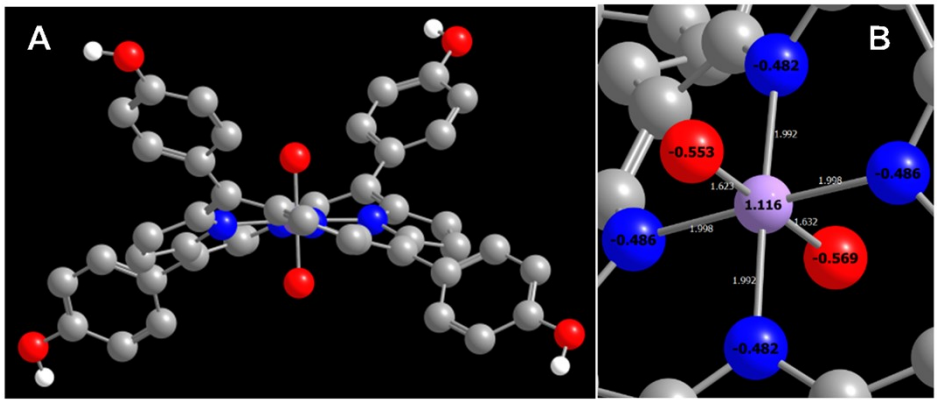

Figure S12. (A) Computed $Mn^{V}THPP(O)_2$ structure and (B) zoom-in on the metal center with selected bond lengths and atomic charges. Black, blue, red, white and purple represent C, N, O, H and Mn atoms, respectively.

Table S1. Computed $Mn^{III}THPP/Mn^{IV}THPP$ redox couple and ligation reactions.

#	Reactions	ΔG^0 (eV)	E^0 (V vs. SHE)
1	$[Mn^{III}THPP(OH)_2]^- \rightarrow [Mn^{IV}THPP(OH)_2]^0 + e^-$		0.46
2	$[Mn^{IV}THPP(OH)_2]^0 + OH^- \rightarrow [Mn^{IV}THPP(O)(OH)]^- + H_2O$	-1.18	
3	$[Mn^{IV}THPP(O)(OH)]^- + OCl^- \rightarrow [Mn^{IV}THPP(O_2)(OH)]^- + Cl^-$	-2.23	

5. Faradaic efficiency calculation

Since the electrochemical oxidation of methane was conducted in a batch electrochemical cell, the faradaic efficiency (FE) of product “i” was calculated by:

$$Q_{output,\,i} = n_i * z * F$$

$$Q_{input} = \int_0^t I(t)dt$$

$$FE_i = \frac{Q_{output}}{Q_{input,i}} * 100\%$$

where $Q_{output,i}$ is the charge involved in the production of product “i”, Q_{input} is the total charge (C) generated by applying a specific potential for a period of time t (sec), n_i is the amount of product “i” generated in the reaction (mole), z is the number of electrons transferred and F is Faraday’s constant (96485 C mole^{-1}). The amount of each product “i” in the gas phase was calculated using a gas chromatograph (GC) calibration curve obtained by a known standard (SCOTTY).

The formation of methane oxygenated products in the solution was verified and quantified by ^{1}H-NMR at the end of the electrolysis. Samples for the analysis were prepared by 0.9 mL of the electrolyte after the experiment, 0.2 mL of D_2O and 0.05 mL 10 mM of DMSO as an internal standard to determine chemical shifts and products concentrations.[10] This analysis was performed with a Bruker AVANCE III 500 MHz spectrometer equipped with a broad band ^{1}H decoupling probe (BBO) at room temperature. Water suppression was achieved using the Bruker pulse program zgpr. A relaxation delay of 10 s was employed, and the number of scans was typically 56.

Quantification was done by the ratio between the areas of the peak related to the product and the peak related to DMSO:

$$[product\ "i"] = \frac{n_{DMSO}}{Vsample} \cdot \frac{area\ of\ product's\ peak \Big/ number\ of\ protons\ in\ the\ product}{area\ of\ DMSO's\ peak \Big/ number\ of\ protons\ in\ DMSO}$$

Example: calculation of the faradaic efficiencies at 1.05 V using the bilayer coating (Ni#/Mn#):

The total charge passed through the setup:

$$Q_{input} = \int_0^t I(t)dt = \int_0^{7200\ s} I(t)dt = 3.469\ C$$

The charge of each product that was detected at the end of the experiment by GC or ^{1}H-NMR (Table S2):

Table S2. The calculated data of the products for Faradaic efficiency calculation.

Detected product	Amount detected [μmole]	Number of electrons passed	The charge involved in the production of the product [C]	Faradaic efficiency [%]
Oxygen	5.2	4	2.007	57.9
Carbon dioxide	0.32	8	0.247	7.1
Formate	1.41	6	0.816	23.5
Methanol	1.96	2	0.378	10.9
			Total Faradaic efficiency [%]	**99.4**

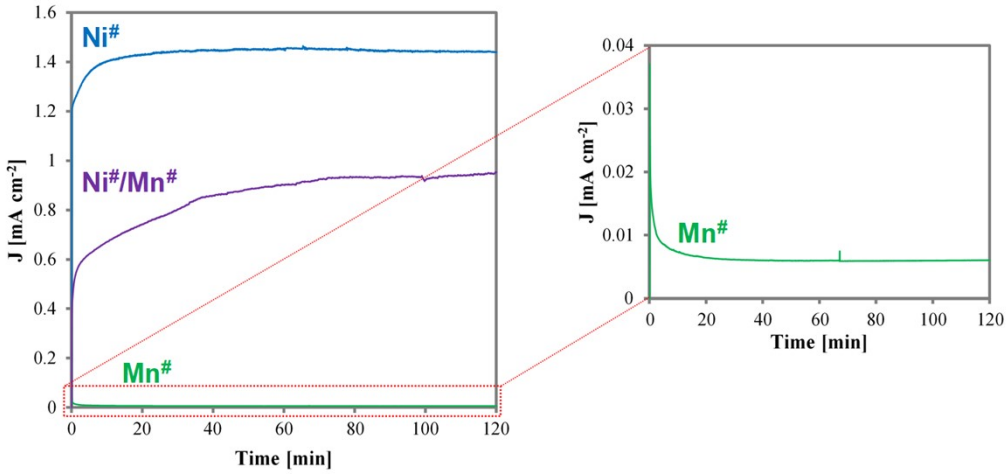

Figure S13. Representative CA curves obtained at 1.05 V with each layer in the presence of methane in 0.1 M KOH.

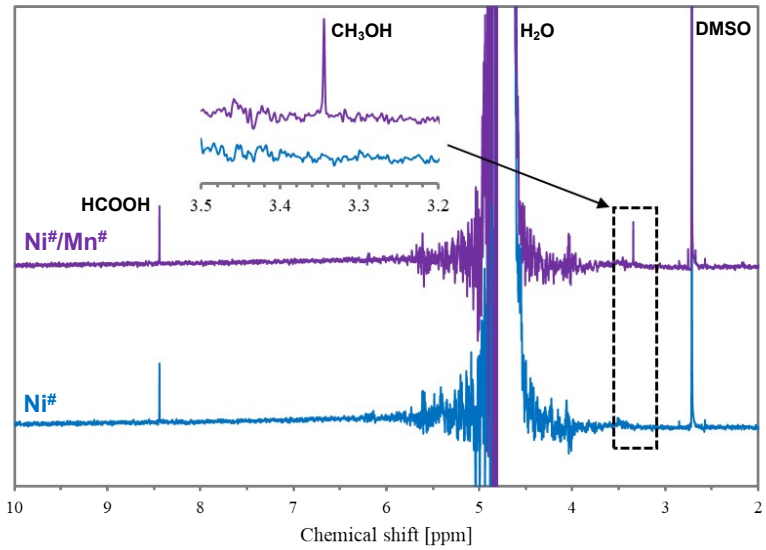

Figure S14. ^{1}H-NMR spectra of the aqueous products. Representative ^{1}H-NMR (500 MHz, in D_2O) spectra obtained in the half-cell configuration at applied potentials of 1.05 V for Ni$^{\#}$ (blue) and Ni$^{\#}$/Mn$^{\#}$ (purple). The solution was analyzed after 2 hours of electrolysis. The peaks at 2.72, 3.34 and 8.44 ppm correspond to DMSO, CH_3OH and HCOOH, respectively.[20]

The electrochemical stability of the bilayer coating was tested by chronoamperometry at 0.95 V in 0.1M KOH for an extended time of 4 hours (Figure S15). A chronoamperogram with a steady state current was obtained without any significant sign of current decay. HRSEM images obtained for the electrode surface after the test showed neither cracks nor ruptures in the coatings. These findings together with the reproducibility of the spectroscopic and electrochemical data concerning the characterization of the films allow us to consider the bilayer configuration to be stable and reliable under the examined conditions.

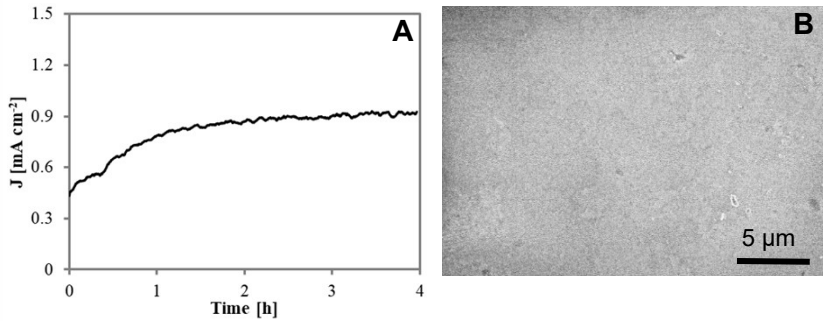

Figure S15. Stability test for the bilayer coating. (A) Stability test performed by CA at 0.95 V in 0.1 M KOH for 4 hours and (B) HRSEM image of the surface of the bilayer Ni$^{\#}$/Mn$^{\#}$ coating after the stability test.

6. CO_2 quantification

When CO_2 is produced in an alkaline electrolyte, it is converted to dissolved carbonate ion. This raises a quantification problem since it cannot be detected in the headspace of the cell. Therefore, we followed a titration procedure in order to quantify the amount of CO_2 formed in the electrochemical reaction.[21]

After applying a chosen potential for 2 h in 0.1 M KOH for products generation, 5 mL of the electrolyte were injected using a syringe into a sealed vial (20 mL) that was purged with He for 1 h prior to the titration procedure. The solution was then titrated by 1 M H_2SO_4 to a pH value of 1 and then the head space was sampled by an air-tight syringe via a septum and analyzed by GC. The concentration of CO_2 was then calculated by a calibration curve, and therefore by using the ideal gas law, we were able to derive the amount of CO_2 dissolved in the electrochemical cell that was generated in the oxidation of methane.

7. References

1 M. S. Wu, C. H. Yang and M. J. Wang, *Electrochimica Acta*, 2008, **54**, 155–161.

2 L. Gu, Y. Wang, R. Lu, L. Guan, X. Peng and J. Sha, *Journal of Materials Chemistry A*, 2014, **2**, 7161–7164.

3 M. S. Wu and C. H. Yang, *Applied Physics Letters*, 2007, **91**, 033109.

4 A. Bettelheim, A. B. White, S. A. Raybuck and R. W. Murray, *Inorg. Chem.*, 1987, **26**, 1009–1017.

5 F. Bruno, M. C. Pham and J. E. Dubois, *Electrochimica Acta*, 1977, **22**, 451–457.

6 P. R. Munroe, *Materials Characterization*, 2009, **60**, 2–13.

7 P. Zhang, J. Hu, B. Liu, J. Yang and H. Hou, *Chemosphere*, 2019, **219**, 617–635.

8 B. Chen, Z. Zhang, S. Kim, M. Baek, D. Kim and K. Yong, *Applied Catalysis B: Environmental*, 2019, **259**, 118017.

9 L. Jiang, M. Li, L. Lin, Y. Li, X. He and L. Cui, *RSC Advances*, 2014, **4**, 26653–26661.

10 Y. Kadosh, E. Korin and A. Bettelheim, *Sustainable Energy and Fuels*, 2021, **5**, 127–134.

11 S. Wang, Z. Wang, Y. Wang, J. Chen, Z. Chen, Y. Chen and J. Fu, *Green Chemistry*, 2019, **21**, 5960–5968.

12 M. J. Frisch, G. W. Trucks, H. B. Schlegel, G. E. Scuseria, M. A. Robb, J. R. Cheeseman, G. Scalmani, V. Barone, G. A. Petersson, H. Nakatsuji, X. Li, M. Caricato, A. V. Marenich, J. Bloino, B. G. Janesko, R. Gomperts, B. Mennucci, H. P. Hratchian, J. V. Ortiz, A. F. Izmaylov, J. L. Sonnenberg, D. Williams-Young, F. Ding, F. Lipparini, F. Egidi, J. Goings, B. Peng, A. Petrone, T. Henderson, D. Ranasinghe, V. G. Zakrzewski, J. Gao, N. Rega, G. Zheng, W. Liang, M. Hada, M. Ehara, K. Toyota, R. Fukuda, J. Hasegawa, M. Ishida, T. Nakajima, Y. Honda, O. Kitao, H. Nakai, T. Vreven, K. Throssell, J. A. Montgomery, Jr., J. E. Peralta, F. Ogliaro, M. J. Bearpark, J. J. Heyd, E. N. Brothers, K. N. Kudin, V. N. Staroverov, T. A. Keith, R. Kobayashi, J. Normand, K. Raghavachari, A. P. Rendell, J. C. Burant, S. S. Iyengar, J. Tomasi, M. Cossi, J. M. Millam, M. Klene, C. Adamo, R. Cammi, J. W. Ochterski, R. L. Martin, K. Morokuma, O. Farkas, J. B. Foresman, and D. J. Fox, Gaussian 16 (Revision A.03) Gaussian, Inc., Wallingford CT, 2016.

13 J. P. Perdew and Y. Wang, *Physical Review B*, 1992, **46**, 12947.

14 R. Krishnan, J. S. Binkley, R. Seeger and J. A. Pople, *The Journal of Chemical Physics*, 2008, **72**, 650.

15 M. Cossi, N. Rega, G. Scalmani and V. Barone, *Journal of Computational Chemistry*, 2003, **24**, 669–681.

16 R. A. Pierotti, *Chemical Reviews*, 1976, **76**, 717–726.

17 F. M. Floris, J. Tomasi and J. L. P. Ahuir, *Journal of Computational Chemistry*, 1991, **12**, 784–791.

18 S. J. Konezny, M. D. Doherty, O. R. Luca, R. H. Crabtree, G. L. Soloveichik and V. S. Batista, *Journal of Physical Chemistry C*, 2012, **116**, 6349–6356.

19 A. E. Reed and F. Weinhold, *The Journal of Chemical Physics*, 1998, **83**, 1736.

20 T. Chatterjee, E. Boutin and M. Robert, *Dalton Transactions*, 2020, **49**, 4257–4265.

21 E. J. McShane, E. J. McShane, A. M. Colclasure, D. E. Brown, D. E. Brown, Z. M. Konz, Z. M. Konz, K. Smith and B. D. McCloskey, *ACS Energy Letters*, 2020, **5**, 2045–2051.